Modeling and simulation of through-focus images for dimensional analysis of nanoscale structures

Xiuguo CHEN[a], Shiyuan LIU[*, b], Chuanwei ZHANG[a], Yuan MA[b], and Jinlong ZHU[b]

[a] Wuhan National Laboratory for Optoelectronics, Huazhong University of Science and Technology, Wuhan 430074, China

[b] State Key Laboratory of Digital Manufacturing Equipment and Technology, Huazhong University of Science and Technology, Wuhan 430074, China

ABSTRACT

In this paper, the through-focus scanning technique using a conventional bright-field optical microscope is introduced for nanoscale dimensional analysis with nanometer sensitivity. This technique uses a set of through-focus image maps (TFIMs) obtained at different focus positions instead of one 'best-focus' image and considers the through-focus image as a unique 'signal' that represents the target. The boundary element method (BEM) and the rigorous coupled-wave analysis (RCWA) method were applied to simulate the optical responses and to obtain the TFIMs of finite aperiodic and infinite periodic structures, respectively. The sensitivity of the through-focus technique for the nanoscale dimensional changes of targets was analyzed by using the differential through-focus image maps (DTFIMs). The simulation results validate the use of this technique for nanoscale metrology.

Keywords: through-focus, nanoscale metrology, boundary element method, rigorous coupled wave analysis, sensitivity

1. INTRODUCTION

With the development of the photolithography process and resolution enhancement technology, traditional very large scale integrated circuits have broken through from micron magnitude to nanometer scale, and it is expected that the critical dimension (CD) could advance towards 45 nm node and beyond. In order to achieve effective process control, fast, inexpensive, nondestructive and reliable nanometer scale feature measurements are extremely useful in semiconductor manufacturing. Currently, CD scanning electron microscopy (CD-SEM) and CD atomic force microscopy (CD-AFM) have been widely used for semiconductor metrology. Although they have the ability to analyze extremely small targets, CD-SEM, for example, has edge detection and modeling requirements and is faced with high costs and throughput concerns, and is in general not well suited for integrated metrology applications. In addition, there is recent research that focuses on evaluating electron beam induced line shrinkage or surface damage effects [1]. In comparison with CD-SEM and CD-AFM, optics based metrology tools have gained more and more attention in semiconductor manufacturing because of their attractive advantages, such as low cost, noncontact, non-destruction, and high throughput. Scatterometry is a non-imaging optical technology that has been used in semiconductor metrology with recent great success. However, some drawbacks of scatterometry are the requirement of a large target size and a repetitive structure, a similar dependence on modeling, and potentially substantial dependence on underlying layers and optical properties [1, 2]. Therefore, improvements in optics-based metrology tools are highly desirable to satisfy the increasing challenges with ever-decreasing dimensions of future technology nodes.

In conventional optical microscopy, the 'best-focus' image is necessary to make a meaningful analysis. This is based on the belief that the most faithful representation of the target is rendered only at the best focus position. Out-of-focus images are in general deemed not particularly useful, especially for metrology applications, to represent the target. During that period in which the wavelength of the light used was much smaller than the size of the critical dimension of the measuring target, these assumptions are quite valid and feasible. But it is hard for optical microscopy to obtain sharp images of the features smaller than half the wavelength of illumination (about 200 nm for the visible region) even at the best focus position, due to the diffraction limit. However, the out-of-focus images do contain useful information regarding the target being measured. In contrast to a single best-focus image, the complete set of out-of-focus images

* Contact author: shyliu@mail.hust.edu.cn; phone: +86 27 87792409; fax: +86 27 87792413.

Sixth International Symposium on Precision Engineering Measurements and Instrumentation, edited by Jiubin Tan, Xianfang Wen, Proc. of SPIE Vol. 7544, 75446C · © 2010 SPIE · CCC code: 0277-786X/10/$18 · doi: 10.1117/12.885232

Downloaded from SPIE Digital Library on 10 Jan 2011 to 211.69.199.26. Terms of Use: http://spiedl.org/terms

contains additional information about the target. This information may be obtained given an appropriate data acquisition and analysis method. In view of the additional information contained in the out-of-focus images, the through-focus scanning technique using a conventional bright-field optical microscope has been introduced recently, which uses a set of through-focus image maps (TFIMs) obtained at different focus positions instead of one 'best-focus' image and considers the through-focus image as a unique 'signal' that represents the target [3]. It is believed that this technique can be used to identify nanoscale variations of targets and to retrieve all the dimensions of an unknown target using a library-matching method.

The TFIMs are formed by stacking the through-focus optical image intensity profiles such that the X-axis represents the actual distance on the target, the Y-axis (or Z-axis) represents the through-focus positions, and the intensity of the image corresponding to each coordinate (x, y) represents the optical intensity. To obtain the TFIMs and simulate the optical responses of through-focus scanning technique for the finite aperiodic and infinite periodic structures, we applied the boundary element method (BEM) and the rigorous coupled-wave analysis (RCWA) method in this paper, respectively. We analyzed the sensitivity of the through-focus scanning technique for the nanometer dimensional changes of targets by using differential through-focus image maps (DTFIMs). The results have validated the use of the through-focus scanning technique for nanoscale measurements.

2. MODELING METHODS

During the last decades, progress in optical modeling including both scalar-based models and vector-based models has occurred. The vector-based optical modeling methods, one of which is the RCWA method, have drawn more and more attention owning to their high accuracy. RCWA obtains the exact solution of Maxwell's equations for electromagnetic diffraction. It arrives at the solution without any approximation and without iterative techniques. It has been widely used for the design of diffractive optical elements (DOEs), and the results have demonstrated that it is currently the most effective method that can be used for the modeling of periodic structures. Therefore, we apply RCWA to simulate the optical response of the through-focus technique for the infinite periodic structures in this paper. However, one great drawback of RCWA is that it has been primarily limited to infinitely periodic structures. As to finite aperiodic targets, it seems to be helpless. To calculate the optical fields of finite aperiodic structures, we apply the boundary element method in this paper. The boundary element method, also known as boundary integral method, is one of the boundary-type methods based on the integral equation method. It is capable of reducing the matrix dimension significantly in comparison with other domain-type methods, such as finite element method (FEM), finite difference method (FDM), and finite-difference time-domain (FDTD). Furthermore, the Sommerfeld's radiation condition can be satisfied implicitly within the BEM's formulation; hence the absorbing boundary conditions (ABCs) are not required for BEM and it is not subject to errors caused by nonphysical backreflections, which is another advantage of BEM over FEM, FDM and FDTD [4].

2.1 BEM for finite aperiodic structures

The geometry of the BEM algorithm for the isolated line diffraction problem is shown in Figure 1(a). Parameters *LH*, *LW*, and *SWA* denote the height, width and side wall angle of the isolated line structure, respectively. To calculate the field reflected from the isolated line target, the space is divided into four homogeneous subregions S_1 to S_4 that are separated by three boundaries Γ_1, Γ_2 and Γ_3, as depicted in Figure 1(b). The refractive index in subregion S_i is denoted by n_i, i = 1, 2, 3, 4. Because n_1 and n_2 correspond to the refractive index of free space, the values of n_1 and n_2 are taken as unity. Subregions S_3 and S_4 correspond to the resist layer and the substrate layer, respectively. A plane wave with unit amplitude is normally incident at boundary Γ_1, which is a dummy boundary that has no effect on the optical field and is only used for modeling conveniently.

Without any loss of generality, we assume that the field values do not change along Z-axis, i.e. $\partial/\partial z = 0$. Then we can get the following two-dimensional Helmholtz equation from Maxwell's equation [5]:

$$\frac{1}{p}\left(\frac{\partial^2\Phi}{\partial x^2}+\frac{\partial^2\Phi}{\partial y^2}\right)+k_0^2 q\Phi = 0 \qquad (1)$$

where $k_0 = \omega\sqrt{\mu_0\varepsilon_0}$. For the transverse electric (TE) mode, $\Phi = E_z$, $p = 1$, $q = \varepsilon$; and for the transverse magnetic

Downloaded from SPIE Digital Library on 10 Jan 2011 to 211.69.199.26. Terms of Use: http://spiedl.org/terms

(TM) mode, $\Phi = H_z$, $p = \varepsilon$, $q = 1$. E_Z and H_Z are the z-components of the electric and magnetic fields, respectively. ε_0 and μ_0 are the permittivity and permeability of the free space, respectively; ε denotes the relative permittivity.

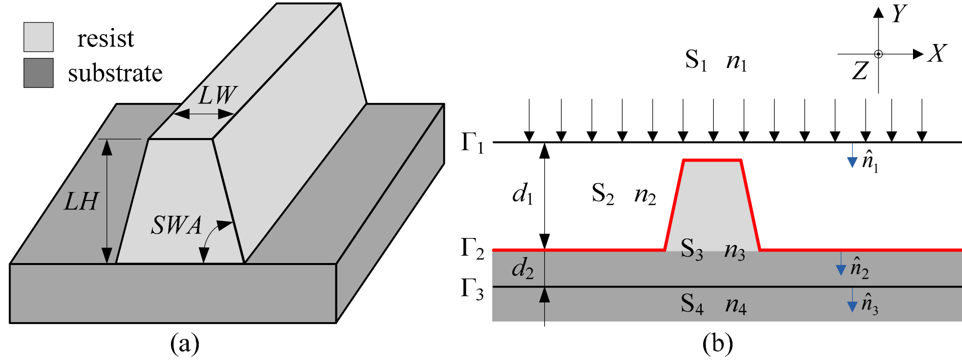

Figure 1. (a) Geometry of BEM algorithm for the isolated line diffraction problem; (b) schematic diagram of the calculated regions with three boundaries Γ_1, Γ_2 and Γ_3.

By applying Green's theorem to equation (1) and taking into account the Sommerfeld radiation condition and the boundary conditions, we can obtain the regional integral equations as follows [6]:

$$\Phi_1^t(r_1) + \int_{\Gamma_1}\left[\Phi_{\Gamma_1}(r'_{\Gamma_1})\hat{n}_1\cdot\nabla G_1(r_1, r'_{\Gamma_1}) - p_1 G_1(r_1, r'_1)\Psi_{\Gamma_1}(r'_{\Gamma_1})\right]dl' = \Phi^{inc}(r_1),\ r_1 \in S_1 \tag{2}$$

$$\begin{aligned}\Phi_2^t(r_2) &- \int_{\Gamma_1}\left[\Phi_{\Gamma_1}(r'_{\Gamma_1})\hat{n}_1\cdot\nabla G_2(r_2, r'_{\Gamma_1}) - p_2 G_2(r_2, r'_{\Gamma_1})\Psi_{\Gamma_1}(r'_{\Gamma_1})\right]dl' \\ &+ \int_{\Gamma_2}\left[\Phi_{\Gamma_2}(r'_{\Gamma_2})\hat{n}_2\cdot\nabla G_2(r_2, r'_{\Gamma_2}) - p_2 G_2(r_2, r'_{\Gamma_2})\Psi_{\Gamma_2}(r'_{\Gamma_2})\right]dl' = 0,\ r_2 \in S_2\end{aligned} \tag{3}$$

$$\begin{aligned}\Phi_3^t(r_3) &- \int_{\Gamma_2}\left[\Phi_{\Gamma_2}(r'_{\Gamma_2})\hat{n}_2\cdot\nabla G_3(r_3, r'_{\Gamma_2}) - p_3 G_3(r_3, r'_{\Gamma_2})\Psi_{\Gamma_2}(r'_{\Gamma_2})\right]dl' \\ &+ \int_{\Gamma_3}\left[\Phi_{\Gamma_3}(r'_{\Gamma_3})\hat{n}_3\cdot\nabla G_3(r_3, r'_{\Gamma_3}) - p_3 G_3(r_3, r'_{\Gamma_3})\Psi_{\Gamma_3}(r'_{\Gamma_3})\right]dl' = 0,\ r_3 \in S_3\end{aligned} \tag{4}$$

$$\Phi_4^t(r_4) - \int_{\Gamma_3}\left[\Phi_{\Gamma_3}(r'_{\Gamma_3})\hat{n}_3\cdot\nabla G_4(r_4, r'_{\Gamma_3}) - p_4 G_4(r_4, r'_3)\Psi_{\Gamma_3}(r'_{\Gamma_3})\right]dl' = 0,\ r_4 \in S_4 \tag{5}$$

$$G_i(r_i, r'_{\Gamma_m}) = \frac{1}{4j}H_0^{(2)}(k_i\left|r_i - r'_{\Gamma_m}\right|),\ i = 1, 2, 3, 4;\ m = i-1, i\ (i>1). \tag{6}$$

where Φ^t, Φ^{inc} are the total and incident field, respectively; $p_i = 1$ for the TE mode and $p_i = n_i^2$ for the TM mode (i = 1, 2, 3, 4); $\hat{n}_i$ denotes the normal unit vector of boundary Γ_i; G_i is the two-dimensional Green's function and $H_0^{(2)}$ is the zero-order Hankel function of the second kind; vectors r_i and r'_{Γ_m} are the position vectors of the points in subregion S_i and at boundary Γ_m, respectively. By matching the tangential electric and magnetic field components at boundary Γ_i, we can obtain the following equations:

$$\Phi_{\Gamma_i}(r_{\Gamma_i}) = \Phi_i^t(r_{\Gamma_i}) = \Phi_{i+1}^t(r_{\Gamma_i}) \tag{7}$$

$$\Psi_{\Gamma_i}(r_{\Gamma_i}) = \left(\frac{1}{p_i}\right)\hat{n}_i\cdot\nabla\Phi_i^t(r_{\Gamma_i}) = \left(\frac{1}{p_{i+1}}\right)\hat{n}_i\cdot\nabla\Phi_{i+1}^t(r_{\Gamma_i}),\ i = 1, 2, 3, 4. \tag{8}$$

In this case, the boundary integral equations may be divided by using a number of nodes at the boundaries $\Gamma_1 - \Gamma_3$, and the field values at these nodes can be determined by using the BEM with quadratic elements. From these discrete values, field values Φ_{Γ_i} and their derivatives Ψ_{Γ_i} of any points r_{Γ_i} at the boundary Γ_i can be calculated by quadratic interpolation. After the boundary values are known, the total field values Φ_i^t of any point r_i in the subregion S_i can be determined by equations (2) - (5).

Downloaded from SPIE Digital Library on 10 Jan 2011 to 211.69.199.26. Terms of Use: http://spiedl.org/terms

The computer memory capacity increases rapidly with the increase in the number of boundaries and sampling points. The BEM algorithm is difficult to implement if many boundaries are involved. To avoid running out of memory when computing, we apply the method proposed by D. Shyu et al. [7] in this paper. By reducing the dimension of the whole boundary matrix, the needed memory capacity for the inverse calculations is decided only by the total number of sampling points and does not depend on the numbers of boundaries.

2.2 RCWA for infinite periodic structures

Without any loss of generality, the RCWA algorithm for the binary rectangular-groove grating diffraction problem depicted in Figure 2 under the condition of TE polarization (the incident electric field is normal to the plane of incident) is analyzed. The algorithm presented here closely follows the formulation presented by M. G. Moharam, et al. [8, 9], wherein the tangential fields are expressed as a Fourier expansion in terms of space harmonics and then electromagnetic boundary conditions are applied at each boundary in the structure.

In the formulation presented here, a linearly polarized light is obliquely incident at an arbitrary angle of incidence θ upon the grating structure. The grating is bounded by two different media with refractive indices n_1 and n_2. The height, width and pitch (period) of the grating line are LH, LW and Λ, respectively. The coordinate system definition is shown in Figure 2. The Z direction is normal to the boundary, and the grating vector is in the X direction.

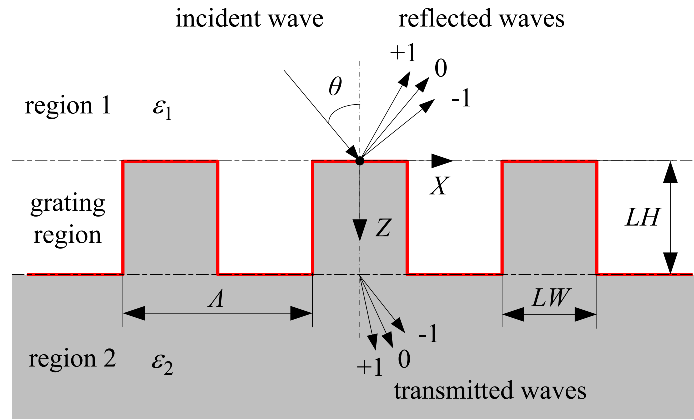

Figure 2. Geometry of RCWA algorithm for the binary rectangular-groove grating diffraction problem.

In the grating region ($0 < z < LH$), the periodic relative permittivity is expandable in a Fourier series of the form:

$$\varepsilon(x) = \varepsilon_1 + (\varepsilon_2 - \varepsilon_1)\sum_p \varepsilon_p \exp(jpKx) \tag{9}$$

where $K = 2\pi/\Lambda$, ε_p is the pth Fourier component of the relative permittivity in the grating region:

$$\varepsilon_h = \frac{1}{\Lambda}\int_0^\Lambda \varepsilon(x)\exp(-jpKx)dx \tag{10}$$

The incident normalized electric field that is normal to the plane of incidence is given by:

$$E_{inc} = \exp\left[-jk_0 n_1 (x\sin\theta + z\cos\theta)\right] \tag{11}$$

where $k_0 = 2\pi/\lambda_0$ and λ_0 is the wavelength of the light in the free space.

According to the Rayleigh expansion, the normalized solution in region 1 ($z < 0$) and region 2 ($z > LH$) are given by:

$$E_1 = E_{inc} + \sum_i R_i \exp\left[-j\left(k_{xi}x - k_{1,zi}z\right)\right] \tag{12}$$

$$E_2 = \sum_i T_i \exp\left\{-j\left[k_{xi}x + k_{2,zi}(z - LH)\right]\right\} \tag{13}$$

Downloaded from SPIE Digital Library on 10 Jan 2011 to 211.69.199.26. Terms of Use: http://spiedl.org/terms

where R_i is the normalized electric-field amplitude of the ith reflected wave in region 1; T_i is the normalized electric-field amplitude of the ith transmitted wave in region 2; k_{xi} is the x-component of the ith diffracted wave and is determined from the Floquet condition:

$$k_{xi} = k_1 \sin\theta - iK \tag{14}$$

$k_{1,zi}$ and $k_{2,zi}$ are the z-component of the ith reflected wave and ith transmitted wave, respectively, and are given by:

$$k_{l,zi}^2 = k_l^2 - k_{xi}^2, \quad l = 1, 2 \tag{15}$$

where the sign of $k_{1,zi}$ is determined by:

$$\mathrm{Re}(k_{l,\mathrm{zi}}) - \mathrm{Im}(k_{l,zi}) \geq 0 \tag{16}$$

The magnetic fields in regions 1 and 2 can be obtained from Maxwell's equation:

$$H = \left(\frac{j}{\omega\mu}\right)\nabla \times E \tag{17}$$

where μ is the permeability of the region and ω is the angular optical frequency.

In the grating region, the tangential electric (y-component) and magnetic (x-component) fields are expressed in Fourier expansions as:

$$E_{gy} = \sum_i S_{yi}(z)\exp(-jk_{xi}x) \tag{18}$$

$$H_{gx} = -j\sqrt{\frac{\varepsilon_0}{\mu_0}}\sum_i U_{xi}(z)\exp(-jk_{xi}x) \tag{19}$$

where ε_0 and μ_0 are the permittivity and permeability of the free space; $S_{yi}(z)$ and $U_{xi}(z)$ are normalized amplitudes of the ith space harmonic fields such that $S_{yi}(z)$ and $U_{xi}(z)$ satisfy Maxwell's equation in the grating region:

$$\frac{\partial E_{gy}}{\partial z} = j\omega\mu_0 H_{gx} \tag{20}$$

$$\frac{\partial H_{gx}}{\partial z} = j\omega\varepsilon_0\varepsilon(x)E_{gy} + \frac{\partial H_{gz}}{\partial z} \tag{21}$$

Substituting (18), (19) into (20), (21) and eliminating H_{gz}, we obtain the coupled-wave equations as follows:

$$\frac{\partial S_{yi}}{\partial z} = k_0 U_{xi} \tag{22}$$

$$\frac{\partial U_{xi}}{\partial z} = \left(\frac{k_{xi}^2}{k_0}\right)S_{yi} - k_0\sum_p \varepsilon_{(i-p)}S_{yp} \tag{23}$$

We can further get the second-order coupled-wave equations from (22) and (23) in a matrix form as:

$$\left[\frac{\partial^2 \mathbf{S}_y}{\partial(z')^2}\right] = [\mathbf{A}][\mathbf{S}_y] \tag{24}$$

where $z' = k_0 z$, and

$$\mathbf{A} = \mathbf{K}_x^2 - \mathbf{E} \tag{25}$$

where $\mathbf{K}_x$ is a diagonal matrix with the diagonal element being equal to k_{xi}/k_0; $\mathbf{E}$ is the matrix formed by the

Downloaded from SPIE Digital Library on 10 Jan 2011 to 211.69.199.26. Terms of Use: http://spiedl.org/terms

permittivity harmonic components, with the i, p element $E_{ip} = \varepsilon_{(i-p)}$; and **I** is an identity matrix. **A**, $\mathbf{K}_x$ and **E** are $n \times n$ matrices, where n is the number of space harmonics retained in the field expansion.

The solution of the space harmonics of the tangential electric fields may be expressed as:

$$S_{yi}(z) = \sum_{m=1}^{n} w_{i,m} \left\{c_m^+ \exp(-k_0 q_m z) + c_m^- \exp[k_0 q_m (z - LH)]\right\} \tag{26}$$

where $w_{i,m}$ and q_m are the elements of the eigenvector matrix **W** and the positive square root of the eigenvalues of the matrix **A**; c_m^+ and c_m^- are unknown constants.

The solution of the space harmonics of the tangential magnetic fields can be derived from (26):

$$U_{xi}(z) = \sum_{m=1}^{n} v_{i,m} \left\{-c_m^+ \exp(-k_0 q_m z) + c_m^- \exp[k_0 q_m (z - LH)]\right\} \tag{27}$$

The quantity $v_{i,m} = w_{i,m} q_m$ is the i, m element of the matrix **V** = **WQ**, where **Q** is a diagonal matrix with the elements q_m.

The amplitudes of the diffracted fields R_i and T_i (together with c_m^+ and c_m^-) are determined by matching the tangential electric and magnetic fields components at the input and transmitted boundaries. At the input boundary (z = 0):

$$\begin{bmatrix} \delta_{i0} \\ jn_1 \delta_{i0} \cos\theta \end{bmatrix} + \begin{bmatrix} \mathbf{I} \\ -j\mathbf{Y}_1 \end{bmatrix} [\mathbf{R}] = \begin{bmatrix} \mathbf{W} & \mathbf{WX} \\ \mathbf{V} & -\mathbf{VX} \end{bmatrix} \begin{bmatrix} \mathbf{c}^+ \\ \mathbf{c}^- \end{bmatrix} \tag{28}$$

and at the transmitted boundary ($z = LH$):

$$\begin{bmatrix} \mathbf{WX} & \mathbf{W} \\ \mathbf{VX} & -\mathbf{V} \end{bmatrix} \begin{bmatrix} \mathbf{c}^+ \\ \mathbf{c}^- \end{bmatrix} = \begin{bmatrix} \mathbf{I} \\ j\mathbf{Y}_2 \end{bmatrix} [\mathbf{T}] \tag{29}$$

where δ_{i0} is the Kronecker delta function; **X**, $\mathbf{Y}_1$ and $\mathbf{Y}_2$ are diagonal matrices, with diagonal elements being equal to $\exp(-k_0 q_m LH)$, $(k_{1,zi}/k_0)$ and $(k_{2,zi}/k_0)$, respectively.

By combining (28) with (29), c_m^+, c_m^-, and the amplitudes of any order diffracted fields R_i and T_i can be determined. After obtaining R_i and T_i, the intensity distribution of the total electromagnetic field in region 1 can be calculated.

For a given RCWA formulation, the accuracy of the solution depends solely on the number of terms in the field space-harmonic expansion, with conservation of energy always being satisfied [9]. In order to achieve higher accuracy, the number of retained order needs to be increased. However, the simulation time increases exponentially with the increase of the number of retained orders. The trade-off between accuracy and computational cost needs to be determined by simulation. According to the analysis of R. M. Silver et al. [10, 11] for the TE mode simulations, 50 orders always achieved convergence, and for the TM mode simulations, 100 orders achieved acceptable convergence in general. Additionally, the RCWA convergence rates are excellent for TE polarization; however, the slow convergence rate always occurs for TM polarization. To improve the convergence rate, the inverse rule proposed by L. Li [12, 13] is applied in this paper.

3. SIMULATION AND SENSITIVITY ANALYSIS

We simulated the optical responses of the through-focus scanning technique for the isolated line structure (as shown in Figure 1) and the binary rectangular-groove grating (as shown in Figure 2) by using BEM and RCWA, respectively. The incident wavelength and the incidence angle used in the simulation process are 530 nm and 0°. The structural parameters of the isolated line and the binary rectangular-groove grating are shown in Table 1. In the isolated line structure, the materials of the resist and substrate layers are Si_3N_4 and silicon, respectively. As to the binary rectangular-groove grating, the region 1 is air and the region 2 is silicon. Therefore, the refractive index of region 1 is 1, and the refractive indices of Si_3N_4 and silicon are 2.0498 and 4.149 – 0.0527i at the 530nm incident wavelength.

Downloaded from SPIE Digital Library on 10 Jan 2011 to 211.69.199.26. Terms of Use: http://spiedl.org/terms

Table 1. The structural parameters of the measuring targets

Target	Line height (nm)	Line width (nm)	Side wall angle (°)	Period (nm)
Isolated line structure	200	50	90°	
Binary rectangular-groove grating	230	152		600

In addition, because the TE mode is generally more sensitive than the TM mode to changes in the dimension of CD, we take TE polarization as the mode of incident light during the simulation. The normalized TFIMs for the isolated line structure and the binary rectangular-groove grating by using BEM and RCWA are shown in Figure 3.

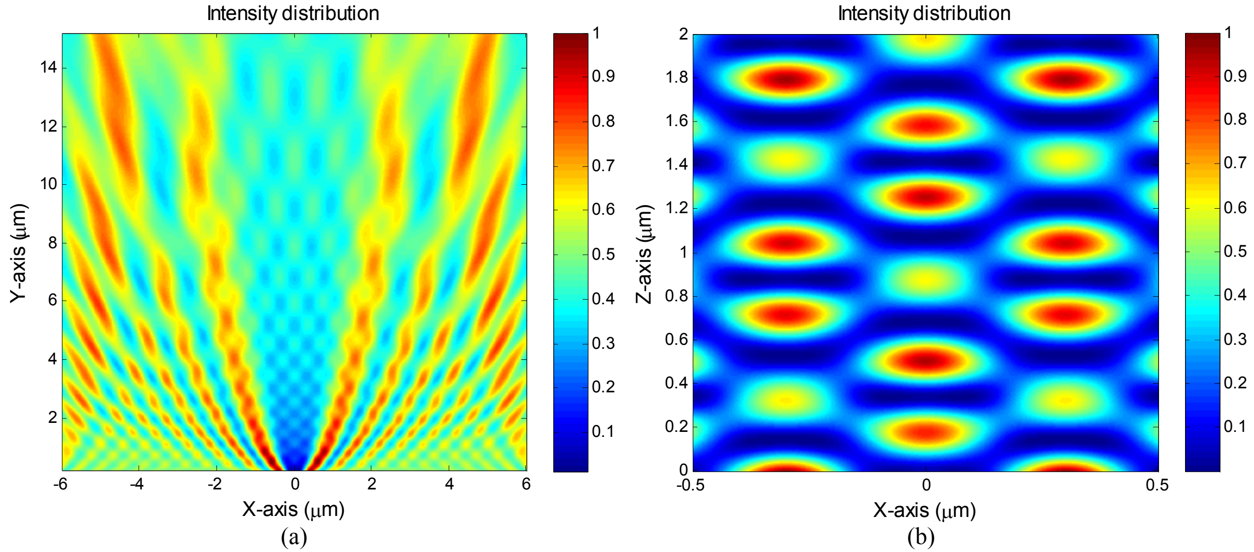

Figure 3. (a) The normalized TFIM of the isolated line structure using BEM; (b) The normalized TFIM of the binary rectangular-groove grating using RCWA. The structural parameters of the isolated line and the binary rectangular-groove grating are shown in Table 1, and the incident wavelength is 530 nm.

To verify the use of the through-focus scanning technique, we analyzed the sensitivity for the nanometer dimensional changes of targets by using the differential through-focus image maps. The DTFIM is defined as the difference between two through-focus image maps. To quantify the difference, we use the moving average (MA) and moving standard deviation (MSD), which are defined as:

$$\mathrm{MA}(y)=\frac{1}{L}\int_L \mathrm{DTFIM}(x,y)\mathrm{d}x \tag{30}$$

$$\mathrm{MSD}(y)=\sqrt{\frac{1}{L}\int_L \left[\mathrm{DTFIM}(x,y)-\mathrm{MA}(y)\right]^2 dx} \tag{31}$$

where x represents the actual distance on the target, L is the range of the target along the X-axis; y represents the through-focus position. MA and MSD show the properties of DTFIM from different aspects. MA is used to represent the average deviation of the original data from the ideal value, and MSD is used to represent the relative deviation of the original data from the average value. The equations of MA and MSD given in (30) and (31) are the continuous forms; however, we can also obtain the discrete forms from (30) and (31) based on the Reimann integration.

DTFIMs of the TFIMs are distinct for different dimensional differences. They enable us to identify which parameter is different between two measuring targets. We applied DTFIMs to evaluate the sensitivity for the nanoscale dimensional changes of the isolated line structure and the binary rectangular-groove grating, and the simulation results are shown in Figure 4. We can easily observe the nanometer scale sensitivity of the through-focus scanning technique from Figure 4. A small change in the dimension of a target produces a markedly corresponding change in the TFIM and DTFIM. The MA and MSD of the DTFIMs for the isolated line structure and the binary rectangular-groove grating are show in Figure

Downloaded from SPIE Digital Library on 10 Jan 2011 to 211.69.199.26. Terms of Use: http://spiedl.org/terms

5, respectively. As shown in Figure 5, we can also find that different parameters show different sensitivities. The line width shows the lowest sensitivity compared with other parameters.

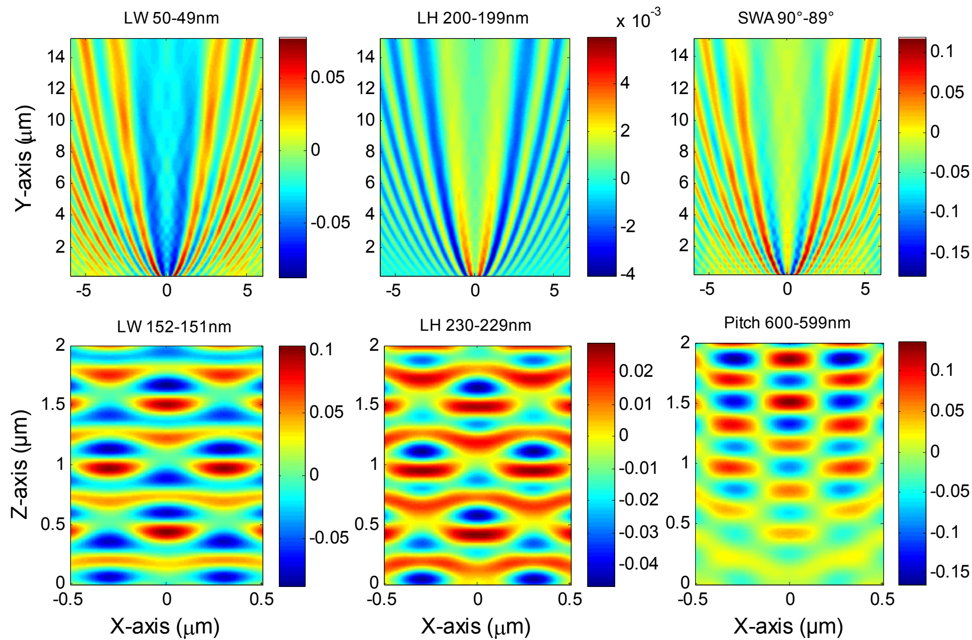

Figure 4. DTFIMs of the isolated line structure and the binary rectangular-groove grating. The upper DTFIMs are for the isolated line structure, and the lower DTFIMs are for the binary rectangular-groove grating. Each DTFIM changes only one parameter and keeps the others the same as in Table 1. There are a one nanometer change in the line height (LH), a one nanometer change in the line width (LW), a one-degree change in the side wall angle (SWA) of the isolated line structure, and a one nanometer change in the pitch of the binary rectangular-groove grating.

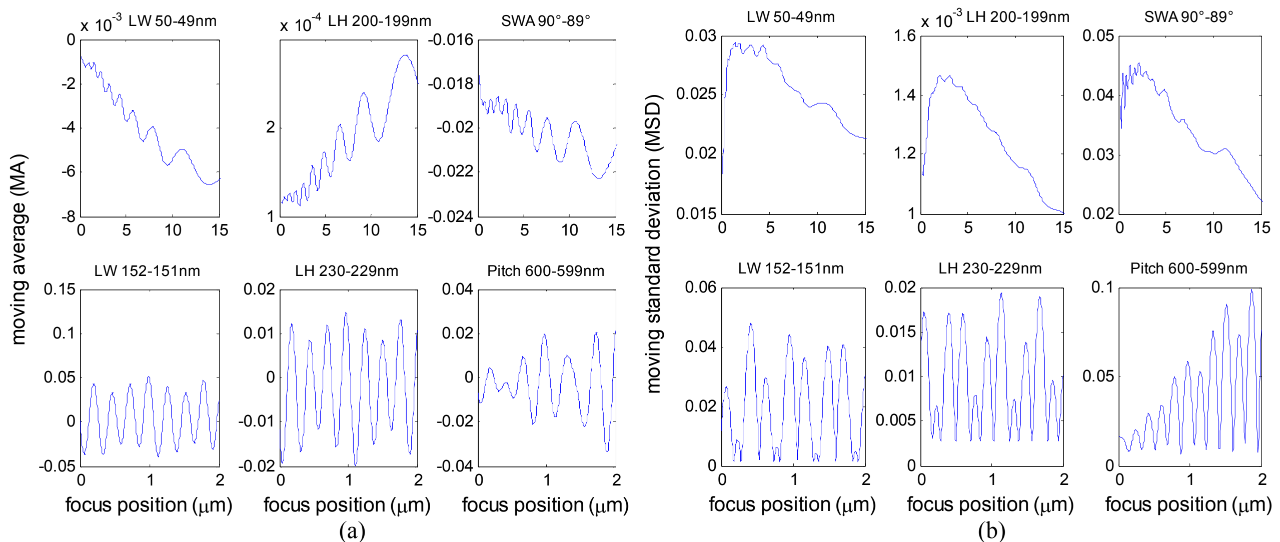

Figure 5. (a) and (b) are the MA and MSD of the measuring targets, respectively. The upper and the lower figures of (a) and (b) are for the isolated line structure and the binary rectangular-groove grating, respectively.

The sensitivity analysis demonstrates the validity of the through-focus scanning technique used for nanoscale measurements. To determine the actual dimensions of an unknown target, it requires a library consists of the simulated TFIMs for all possible combinations of the target dimensions under the given experimental conditions. The experimental TFIM of the unknown target can then be compared with the library. The simulated TFIM from the library that best matches the experimental TFIM provides the dimensions of the measuring target.

Downloaded from SPIE Digital Library on 10 Jan 2011 to 211.69.199.26. Terms of Use: http://spiedl.org/terms

4. CONCLUSIONS

In this paper, the through-focus scanning technique using a conventional bright-field optical microscope is introduced for nanoscale dimensional analysis with nanometer sensitivity. This technique uses a set of TFIMs obtained at different focus positions instead of one 'best-focus' image and considers the through-focus image as a unique 'signal' that represents the target. The optical responses of the through-focus scanning technique for the finite aperiodic and infinite periodic structures are simulated by using BEM and RCWA, respectively. We analyzed the sensitivity of the through-focus scanning technique for the nanometer dimensional changes of targets based on DTFIMs. The results have validated the use of the through-focus scanning technique for nanoscale measurements. The investigation in this paper shows that the through-focus scanning technique provides a promising nondestructive metrology technique for nanoscale structures with the potential of measuring multiple parameters and replacing conventional time-consuming and expensive measurement methods. We expect that the through-focus scanning technique may be applicable to a wide variety of targets with a variety of applications, such as CD metrology, overlay metrology, defect analysis, and process control. It may be also applicable to many application areas, such as nanomanufacturing, semiconductor process control, and biotechnology.

ACKNOWLEDGEMENTS

This work was supported by National Natural Science Foundation of China (Grant No. 91023032, 51005091, 50775090), National Hi-Tech Research and Development Program of China (Grant No. 2006AA04Z325), and China Postdoctoral Science Foundation (Grant No. 20100470052).

REFERENCES

[1] R. M. Silver, R. Attota, M. Stocker, M. Bishop, L. Howard, T. Germer, E. Marx, M. Davidson, and R. Larrabee, "High-resolution optical metrology," Proc. SPIE **5752**, 67-79 (2005).

[2] R. Attota, R. M. Silver, and B. M. Barnes, "Optical through-focus technique that differentiates small changes in line width, line height and sidewall angle for CD, overlay, and defect metrology applications," Proc. SPIE **6922**, 69220E (2008).

[3] R. Attota, T. A. Germer, and R. M. Silver, "Through-focus scanning-optical-microscope imaging method for nanoscale dimensional analysis," Opt. Lett. **33**, 1990-1992 (2008).

[4] D. W. Prather, M. S. Mirotznik, and J. N. Mait, "Boundary integral methods applied to the analysis of diffractive optical elements," J. Opt. Soc. Am. A **14**, 34-43 (1997).

[5] M. Koshiba and M. Suzuki, "Application of the boundary-element method to waveguide discontinuities," IEEE T. Microw. Theory **34**, 301-307 (1986).

[6] D. Shyu, M. Lu, and C. Ko, "High-resolution through-focus metric with two-pitch grating target," Opt. Commun. **276**, 31-36 (2007).

[7] D. Shyu and M. Lu, "Analysis of the through-focus images with boundary-element method in high resolution optical metrology," Rev. Sci. Instrum. **77**, 103703 (2006).

[8] M. G. Moharam and T. K. Gaylord, "Rigorous coupled-wave analysis of planar-grating diffraction," J. Opt. Soc. Am. **71**, 811-818 (1981).

[9] M. G. Moharam, E. B. Grann, and D. A. Pommet, "Formulation for stable and efficient implementation of the rigorous coupled-wave analysis of binary gratings," J. Opt. Soc. Am. A **12**, 1068-1076 (1995).

[10] R. M. Silver, T. Germer, R. Attota, B. M. Barnes, B. Bunday, J. Allgair, E. Marx, and J. Jun, "Fundamental limits of optical critical dimension metrology: a simulation study," Proc. SPIE **6518**, 65180U (2007).

[11] R. M. Silver, R. Attota, and E. Marx, "Model-based analysis of the limits of optical metrology with experimental comparison," Proc. SPIE **6617**, 66170W (2007).

[12] L. Li, "Use of Fourier series in the analysis of discontinuous periodic structures," J. Opt. Soc. Am. A **13**, 1870-1876 (1996).

[13] L. Li, "Formulation and comparison of two recursive matrix algorithms for modeling layered diffraction gratings," J. Opt. Soc. Am. A **13**, 1024-1035 (1996).

Downloaded from SPIE Digital Library on 10 Jan 2011 to 211.69.199.26. Terms of Use: http://spiedl.org/terms